Geochemistry Geophysics Geosystems G3

Article
Volume 13, Number 1
29 September 2012
Q0AO01, doi:10.1029/2012GC004148
ISSN: 1525-2027

Published by AGU and the Geochemical Society

Multiproxy characterization and budgeting of terrigenous end-members at the NW African continental margin

Janna Just
MARUM – Center for Marine and Environmental Sciences and Faculty of Geosciences, University of Bremen, PO Box 330440, DE-28334 Bremen, Germany (janna.just@uni-bremen.de)

David Heslop
Research School of Earth Sciences, Australian National University, Canberra, ACT 0200, Australia (david.heslop@anu.edu.au)

Tilo von Dobeneck and Torsten Bickert
MARUM – Center for Marine and Environmental Sciences and Faculty of Geosciences, University of Bremen, PO Box 330440, DE-28334 Bremen, Germany (dobeneck@uni-bremen.de; tbickert@marum.de)

Mark J. Dekkers
Paleomagnetic Laboratory "Fort Hoofddijk," Department of Earth Sciences, Faculty of Geosciences, Utrecht University, Budapestlaan 17, NL-3584 CD Utrecht, Netherlands (m.j.dekkers@uu.nl)

Thomas Frederichs
MARUM – Center for Marine and Environmental Sciences and Faculty of Geosciences, University of Bremen, PO Box 330440, DE-28334 Bremen, Germany (frederichs@uni-bremen.de)

Inka Meyer
MARUM – Center for Marine and Environmental Sciences and Faculty of Geosciences, University of Bremen, PO Box 330440, DE-28334 Bremen, Germany

Now at Alfred Wegener Institute for Polar and Marine Research, 25 Am Handelshafen 12, DE-27570 Bremerhaven, Germany (minka@marum.de)

Matthias Zabel
MARUM – Center for Marine and Environmental Sciences and Faculty of Geosciences, University of Bremen, PO Box 330440, DE-28334 Bremen, Germany (mzabel@uni-bremen.de)

[1] Grain-size, terrigenous element and rock magnetic remanence data of Quaternary marine sediments retrieved at the NW African continental margin off Gambia (gravity core GeoB 13602–1, 13°32.71′N, 17°50.96′W) were jointly analyzed by end-member (EM) unmixing methods to distinguish and budget past terrigenous fluxes. We compare and cross-validate the identified single-parameter EM systems and develop a numerical strategy to calculate associated multiparameter EM properties. One aeolian and two fluvial EMs were found. The aeolian EM is much coarser than the fluvial EMs and is associated with a lower goethite/hematite ratio, a higher relative concentration of magnetite and lower Al/Si and Fe/K ratios. Accumulation rates and grain sizes of the fluvial sediment appear to be primarily constrained by shore distance (i.e., sea level fluctuations) and to a lesser extent by changes in hinterland precipitation. High dust fluxes occurred during the Last Glacial Maximum (LGM) and during Heinrich Stadials (HS) while the fluvial input remained unchanged. Our approach reveals that the LGM dust fluxes were ~7 times higher than today's.

However, by far the highest dust accumulation occurred during HS 1 (~300 g m^{-2} yr^{-1}), when dust fluxes were ~80 fold higher than today. Such numbers have not yet been reported for NW Africa, and emphasize strikingly different environmental conditions during HSs. They suggest that deflation rate and areal extent of HSs dust sources were much larger due to retreating vegetation covers. Beyond its regional and temporal scope, this study develops new, in principle, generally applicable strategies for multimethod end-member interpretation, validation and flux budgeting calibration.

Components: 10,600 words, 9 figures, 2 tables.

Keywords: end-member; modeling; multiproxy; paleoclimate.

Index Terms: 0473 Biogeosciences: Paleoclimatology and paleoceanography (3344, 4900); 1512 Geomagnetism and Paleomagnetism: Environmental magnetism; 1622 Global Change: Earth system modeling (1225, 4316).

Received 14 March 2012; **Revised** 16 August 2012; **Accepted** 21 August 2012; **Published** 29 September 2012.

Just, J., D. Heslop, T. von Dobeneck, T. Bickert, M. J. Dekkers, T. Frederichs, I. Meyer, and M. Zabel (2012), Multiproxy characterization and budgeting of terrigenous end-members at the NW African continental margin, *Geochem. Geophys. Geosyst.*, *13*, Q0AO01, doi:10.1029/2012GC004148.

Theme: Magnetism From Atomic to Planetary Scales: Physical Principles and Interdisciplinary Applications in Geosciences and Planetary Sciences

1. Introduction

[2] Climate reconstructions of arid and humid conditions during the geological past can be obtained by investigation of sedimentary proxy records. Variations in Quaternary terrigenous element ratios and grain-size distributions of NW African continental margin sediments have been linked to changes in fluvial and aeolian inputs, which are in turn associated with fluctuations of continental humidity [*Schneider et al.*, 1997; *Zabel et al.*, 2001] and wind strength [*Koopmann*, 1981; *Sarnthein et al.*, 1981; *Matthewson et al.*, 1995; *Holz et al.*, 2007]. Palynological analyzes of vegetation types [*Bouimetarhan et al.*, 2009] and the isotopic composition of plant waxes in marine sediments [*Schefuß et al.*, 2005; *Castanñda et al.*, 2009; *Niedermeyer et al.*, 2010; *Collins et al.*, 2011] have been used to reconstruct past vegetation distributions.

[3] On glacial-interglacial time scales, climatic conditions in NW Africa changed significantly. Reconstructions from marine sediment cores [*Sarnthein et al.*, 1981; *Balsam et al.*, 1995; *Matthewson et al.*, 1995; *Kohfeld and Harrison*, 2001; *Larrasoaña et al.*, 2003] supported by numerical modeling [*Mahowald et al.*, 1999, 2006] indicate that the dust input to the North Atlantic Ocean was substantially higher during the Last Glacial Maximum (LGM) compared to recent times. This phenomenon was linked to higher wind speeds [*Sarnthein et al.*, 1981; *Matthewson et al.*, 1995; *Ruddiman*, 1997] and enhanced deflation due to reduced vegetation cover [*Mahowald et al.*, 1999]. Pollen distributions in marine sediments indicate that wind strength was intensified during late Quaternary cold stages. Especially during the LGM, trade winds were blowing in a more southerly direction than at present [*Hooghiemstra et al.*, 2006, and references therein]. Also, paleohydrological proxy data indicate arid conditions on the continent during the LGM [e.g., *Gasse*, 2000, 2001, 2006].

[4] Large North Atlantic freshwater releases during Heinrich Stadials (HS) induced a slow-down of the meridional overturning circulation causing a short-term southward displacement of the Inter Tropical Convergence Zone (ITCZ) and an associated contraction of the African rain belt [*Mulitza et al.*, 2008; *Itambi et al.*, 2009; *Collins et al.*, 2011]. This resulted in more arid conditions in Northern Africa, in particular in the modern Sahel Belt, and intensified zonal winds at the level of the African Easterly Jet (AEJ) [*Mulitza et al.*, 2008].

[5] Episodic phases of humid conditions occurred in the Sahara during the Late Pleistocene and the early Holocene resulting in a dense vegetation cover [*Sarnthein*, 1978; *COHMAP Members*, 1988; *deMenocal et al.*, 2000a, 2000b; *Castañeda et al.*, 2009]. The latest of these so-called African Humid periods (AHP) lasted from 14.8 ka to about 5.5 ka and was only interrupted by the Younger Dryas stadial at ~12 ka [*deMenocal et al.*, 2000b].

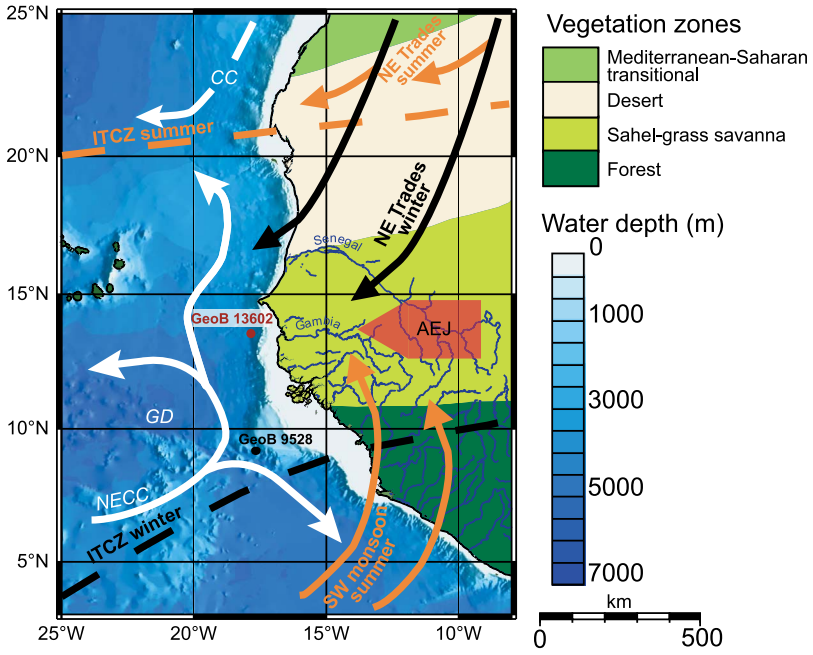

Figure 1. Vegetation belts on the NW African continent [modified after *White*, 1983]. Oceanic surface circulation (white arrows) is controlled by the North Equator Counter Current (*NECC*) and associated anticyclonic circulation around the Guinea Dome (*GD*) and by the Canary Current (*CC*). Orange and black arrows indicate atmospheric features during summer and winter, respectively. Gravity core GeoB 13602–1 (studied here) is depicted in red and GeoB 9528–3 [*Castañeda et al.*, 2009] in black.

[6] While the timing, scale, and causes of these massive climate changes in NW Africa are well established, it is still difficult to estimate related changes in dust flux and river runoff during the highly contrasting climate periods of the past 80 kyrs. The transport pathways, fractionation processes, and post-depositional alterations must be understood as they all may significantly modify the fingerprint of the source. It is best practice to compare and cross-validate proxy-based terrigenous flux reconstructions from several, not intrinsically correlated parameters.

[7] In this study we investigate core material retrieved from the W African continental margin in the corridor between the present ITCZ summer and winter positions (Figure 1). Because of the location of the studied core, we expect that the terrigenous material is supplied predominantly by the Gambia River and the prevailing wind systems (NE Trades, AEJ). Grain-size, geochemical and rock-magnetic data have been combined because they reflect transport and source characteristics from different perspectives and can be obtained by rapid, automated measurements.

[8] We introduce an innovative multivariate strategy combining single parameter end-member (EM) analysis and least squares fitting to determine associated multiproxy EM characteristics. This approach enables a cross-validation and joint interpretation of the EM systems. Based on the multiproxy characteristics, we assess the influence of transport, environmental change, and source area variability on the different EM properties. Our approach allows us to calculate mass accumulation rates of fluvial and aeolian sediments at our study site providing a high-resolution record of past terrigenous flux changes.

1.1. Materials

[9] Gravity core GeoB 13602–1 (13°32.71′N; 17°50.96′W) was retrieved during RV *Maria S. Merian* Cruise MSM 11/2 in 2009 from the continental slope off Gambia in a water depth of 2,395 m (Figure 1). In this area the westward deflected surface Canary Current converges with the North Equatorial Counter Current (Figure 1). The northward flowing South Atlantic Central Water (SACW) extends between 300 and 600 m water depth; at deeper levels southward flowing North Atlantic Deep Water is present [*Tomczak*, 2003].

[10] The 8.75 m long sediment core consists of hemipelagic dark olive clays and silts; a significant change to reddish brownish colors is observed in the depth interval 2.00–2.85 m. The sediment is

undisturbed except for a small scale distal turbidite at 3.90–4.00 m depth.

[11] Gravity core GeoB 13602–1 was sampled at 5 cm intervals. All samples were freeze-dried before analysis. An age model for this core by *Just et al.* [2012] is based on correlation of the oxygen isotope record of epibenthic *Cibicoides wuellestorfi* to that of MD 95–2042 [*Shackleton et al.*, 2000] and five radiocarbon ages (see auxiliary material).[1] For the age-model construction the depth interval of the turbidite was excluded. GeoB 13602–1 spans the last 76 ka and thus Marine Isotope Stages (MIS) 1 through 4 and the end of MIS 5. The averaged sedimentation rate is ~11 cm kyr^{-1} and, accordingly, sampling at 5 cm intervals corresponds to a mean resolution of 450 years and permits the resolution of millennial scale climatic variations such as HSs.

1.2. Source Areas and Transport of Terrigenous Material

[12] Two main source areas for the mobilization of aeolian dust from N Africa have been identified: The Bodélé Depression in Chad, which represents at present the most productive dust source in the world [*Prospero et al.*, 2002], and an area in northern Mali and Mauretania where emissions are less intense but the area is much larger than the Bodélé Depression [*Engelstaedter et al.*, 2006].

[13] Dry and deep atmospheric convection initiates near-surface turbulence and suspends soil particles [*Engelstaedter et al.*, 2006]. Dust is uplifted by vertical convection and transported westward within the Saharan Air Layer by the AEJ [e.g., *Pye*, 1987]. Coarse, more proximal dust is transported to the Atlantic Ocean by NE trade winds mainly during winter [e.g., *Sarnthein et al.*, 1981; *Prospero*, 1996]. The relative contributions of these two transport mechanisms are still a matter of debate.

[14] The Gambia River originates in Eastern Senegal and has only a few small contributories. It flows in a westerly direction through Senegal and Gambia to the Atlantic Ocean. The drainage basin comprises an area of 78,000 km^2 and is dominated by savanna vegetation types [*Lesack et al.*, 1984] (cf. Figure 1). With respect to other rivers in NW Africa, e.g., the Senegal River, whose drainage basin is 3.5 times wider and covers different vegetation zones, the fluvial discharge of the Gambia reflects regional changes in precipitation and mirrors the geology of the drainage basin and most importantly their pedogenic products.

[15] Outcrops of the West African Shield consist of metamorphic schists, basic volcanics, sedimentary rocks, and granites. In the SE of the drainage area these formations are overlain by Paleozoic metamorphic schists and quartzites, sandstones and dolomites. Locally, dolerites and rhyolites are present. In the western part of the drainage area, Mesozoic to Tertiary sediments are found [*Lesack et al.*, 1984, and references therein]. In the northern part of the catchment, ferruginous soils with typical assemblages of kaolinitic and minor illitic clays with low organic matter occur. Further to the south, ferralitic soils are dominated by kaolinite and iron and aluminum oxides, with a high organic matter content [*Lesack et al.*, 1984; *FAO et al.*, 2009, and references therein].

[16] A further component, which may contribute to the fluvial load, is material advected from farther south (e.g., Geba River in Guinea-Bissau). However, since the current velocities are moderate [*Just et al.*, 2012, Figure 1b], it is reasonable to assume that such advected material makes only a minor contribution to the sediment reaching the study site.

2. Methods

2.1. Geochemistry

[17] For geochemical analyses, 4–5 g of freeze-dried sediment samples were homogenized. The elemental composition was measured by energy dispersive polarization X-ray fluorescence spectroscopy using a SPECTRO XEPOS instrument [*Wien et al.*, 2005]. Quality control was assessed by repeated measurements of standard reference material MAG-1 [*Govindaraju*, 1994]. For a complete description see *Mulitza et al.* [2008].

2.2. Grain-Size Analysis

[18] To analyze the grain-size distribution of the lithic fraction, the biogenic compounds were removed from the sediment. Organic matter was removed by boiling 0.5 g of bulk sediment with H_2O_2 (35%). Afterwards, the sample was boiled with HCl (10%) and demineralized water to remove $CaCO_3$. The amount of opal is relatively low (1–5 weight %, data not shown) and was not dissolved. After the above procedure, the approximate terrigenous fraction is obtained. Grain-size distributions were measured using a Beckman Coulter laser particle sizer LS200 in 92 logarithmically spaced size classes ranging

[1] Auxiliary materials are available in the HTML. doi:10.1029/2012GC004148.

from 0.39 to 2000 μm. Grains coarser than 133 μm are not present in the samples. For the later end-member unmixing and visualization the 64 fractions from 0.39 to 133 μm were pooled into 32 size classes to smooth the data.

2.3. Rock Magnetic Analyses

[19] Isothermal remanent magnetization (IRM) acquisition curves are indicative for the magnetic mineral assemblage and the concentration of the different minerals. *Just et al.* [2012] measured IRM acquisition curves using an automated 2-G Enterprises 755R DC superconducting magnetometer for fields up to 700 mT and by using an "external" pulse magnetizer (2-G Enterprises) for fields up 2700 mT. For further detail see *Just et al.* [2012].

2.4. Dry Bulk Density and Mass Accumulation Rates

[20] To determine the dry bulk density and estimate the mass fraction of terrigenous sediments, 10 cm^3 of sediment were freeze-dried and weighed. Mass accumulation rates (MARs, m_{TOT}) are calculated by multiplication of dry bulk density and sedimentation rate. The terrigenous MARs (m_{TER}) were calculated by subtracting the biogenic (carbonate) mass fractions (c_{BIO}, data from *Just et al.* [2012], see Figure S1 in the auxiliary material):

$$m_{TER} = m_{TOT} * (1 - c_{BIO}). \quad (1)$$

2.5. End-Member Analysis

[21] Downcore measurements of element concentrations, grain-size distributions, and IRM acquisition curves (adopted from *Just et al.* [2012]) reflecting mixtures of different source materials were unraveled by EM unmixing. The employed algorithm was developed by *Heslop and Dillon* [2007] based on an approach similar to that of *Weltje* [1997]. Under the assumption of linear mixing, such an EM mixing system can be written in matrix notation as

$$\boldsymbol{X} = \boldsymbol{AS} + \boldsymbol{E} \quad (2)$$

where $\boldsymbol{X}$ represents the n-by-m data matrix of n samples (one per row) and m variables (e.g., grain-size classes, relative element abundances) in the columns. Matrix $\boldsymbol{A}$ (n by l) denotes the abundance of l EMs (one per column) for each sample (one per row). Matrix $\boldsymbol{S}$ represents the m properties of the l EMs, and $\boldsymbol{E}$ is the error matrix of residuals. Because the contributions of each EM have to be positive and the variables (e.g., grain-size classes, elemental abundances) of each EM must add up to ones, non-negativity constraints ($\boldsymbol{A} \geq 0$; $\boldsymbol{S} \geq 0$) and a sum-to-one constraint for the rows in $\boldsymbol{S}$ and $\boldsymbol{A}$ are included in the unmixing algorithm.

[22] Residuals of the EM model include instrumental noise, compositional variations of the individual sources over time and non-identified additional sources that were not detected due to low or only brief activity. Before performing the unmixing, low-rank representations and their coefficients of determination (R^2) with the input data are calculated by principal component analysis (PCA). The decision on the number of EMs to include in the final mixing model is a compromise between keeping the number of components low while maintaining a reasonably good approximation of the input data. Additionally, the number of EMs should also be reasonable in the geological context of the study [*Weltje*, 1997; *Weltje and Prins*, 2007]. For a more detailed description about the mathematical approach of the algorithm we refer the reader to *Weltje* [1997] and *Heslop and Dillon* [2007].

[23] For performing the EM unmixing of the geochemical data set, the mass concentrations of the most abundant 'terrigenous' elements Mg, Al, Si, K, Ti, Fe were normalized to a sum of 1. Since we are only interested in the terrigenous fraction, Ca was excluded as it is highly correlated with the biogenic fraction.

3. Results

3.1. Geochemistry

[24] Three different element ratios (Al/Si, Ti/Fe, Fe/K) are used to characterize the downcore variations in chemical composition (Figure 2). The Al/Si and Fe/K ratios of terrigenous sediments reflect the degree of weathering of the terrigenous sediment components [*Govin et al.*, 2012]. Because of its association to heavy minerals, the Ti (here normalized to Fe) content is indicative of physical grain-size. It was shown that off NW Africa these elemental ratios are distinctively different for aeolian and fluvial material [*Gac and Kane*, 1986; *Chiapello et al.*, 1997; *Moreno et al.*, 2006] (cf. Table 1). Glacial stages MIS 2 and MIS 4 have lower Al/Si and Fe/K and slightly elevated Ti/Fe ratios in comparison with MIS 1 and MIS 3. The MIS 4/3 and MIS 2/1 transitions are sharp, while the MIS 3/2 transition is more smooth. Al/Si and Fe/K rather gradually decrease from the beginning of MIS 3 until MIS 2, whereas Ti/Fe remains stable.

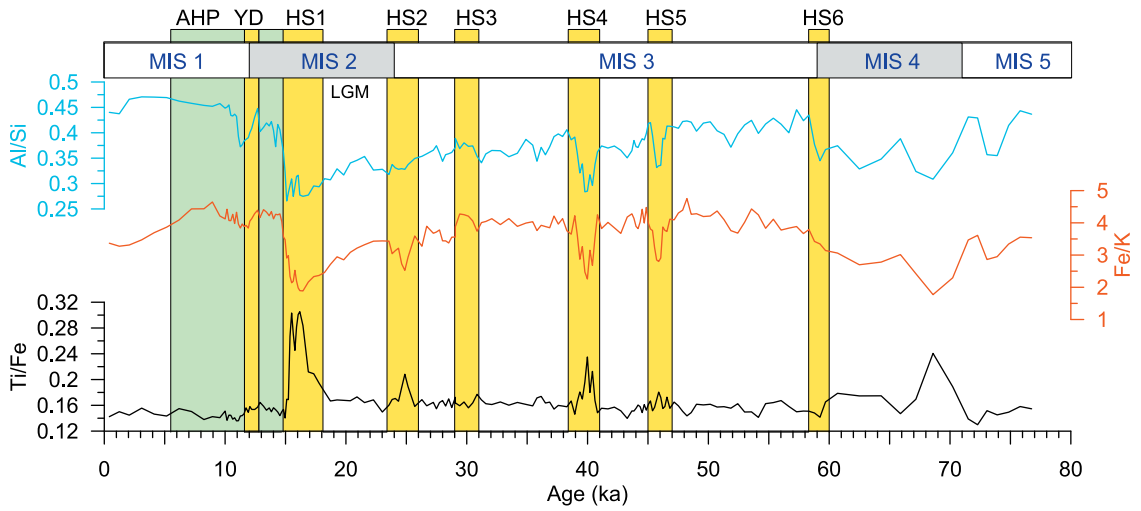

Figure 2. Elemental ratios of GeoB 13602–1. Minima in Al/Si and Fe/K ratios and maxima in Ti/Fe ratios denote dry conditions on the African continent. MIS: Marine Isotope Stage, LGM: Last Glacial Maximum, HS: Heinrich Stadial, YD: Younger Dryas, AHP: African Humid Period. HSs are adopted from the timing of Heinrich Events [*Sarnthein et al.*, 2001].

[25] Remarkably low values mark HS 5, 4 and 2 in the Fe/K and Al/Si records. Ti/Fe shows significant peaks only during HS 2 and 4. HS 1 is characterized by the most extreme values of all reported element ratios. It is marked by a sharp increase in Ti/Fe at its beginning. Notably, however, Al/Si and Fe/K show a more gradual decrease than the corresponding increase in Ti/Fe. Furthermore, all element ratios show a characteristic double peak and trough, respectively. The Younger Dryas (YD) is expressed by lower Al/Si and Fe/K and slightly elevated Ti/Fe ratios. A drop in Fe/K occurs at the end of the African Humid Period (AHP) around 6 ka.

3.2. Grain-Size Distribution

[26] Since off NW Africa the grain-sizes of fluvial material are finer compared to aeolian dust [*Koopmann*, 1981], coarsening and fining grain sizes correspond to increasing proportions of aeolian and fluvial material, respectively.

[27] Generally, a bimodal grain-size distribution prevails throughout the record (Figure 3). One fraction spans grain-size classes from 2 to 20 μm, the other one comprises coarser grain sizes between 25 and 90 μm. During late MIS 5, sediments are relatively uniform and fine, while from MIS 4 to MIS 1 two modes are distinct. During MIS 3 and MIS 1 the distribution is dominated by the finer grain-size classes while MIS 2 has coarser fractions. In the Holocene, the coarse fraction is entirely missing, and sediments are mostly finer than 9 μm. Intervals of significant coarse modes correspond to HS 5, HS 4, HS 2, the LGM and HS 1.

3.3. Differences and Similarities in Proxy Records

[28] The general patterns in all proxy records correspond to environmental changes between dry and humid conditions, i.e., high contributions of aeolian and fluvial material, respectively. These climatic changes are inferred from decreasing Al/Si and

Table 1. Elemental Ratios of Dust and Fluvial Material off NW Africa[a]

Sample	Al/Si	Fe/K	Ti/Fe	Reference
Dust Cap Verdes (Sal Island)	0.49	2.82		*Chiapello et al.* [1997]
	0.45	2.31		
	0.43	2.09		
HAR (aeolian deposit)	0.21	2.71	0.17	*Moreno et al.* [2006]
MON (aeolian deposit)	0.19	3.10	0.27	
Senegal	0.54	4.77	0.08	*Gac and Kane* [1986]

[a]The abbreviations correspond to aeolian deposits in SW Niger by northeasterly winter Harmattan (HAR) and southwesterly summer monsoon (MON) winds.

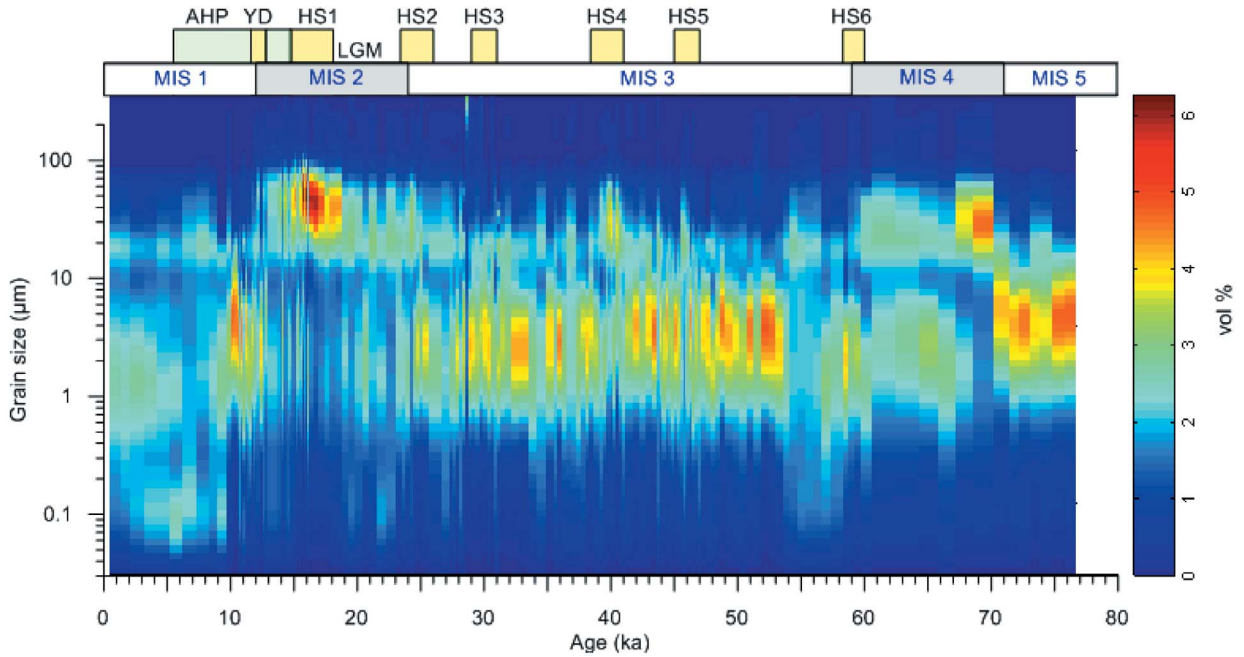

Figure 3. Grain-size data of GeoB 13602–1. Two modes of grain sizes are apparent. The fine mode corresponds to grains finer than 10 μm, the coarser mode is composed of grains in the range of 20–70 μm. During dry periods, in MIS 2 and the HSs, the sediments are coarser. For abbreviations see Figure 2.

Fe/K ratios and a coarsening of grain size. Additionally, in GeoB 13602–1 the Ti/Fe ratio appears to be a significant indicator of higher aeolian input since Ti is enriched in coarse sediments [*Boyle*, 1983; *Zabel et al.*, 1999] (cf. Table 1). The most striking features in all parameter sets are the peaks that occur during HSs. These features support earlier findings of dry conditions in NW Africa during cold periods in the northern N Atlantic [*Jullien et al.*, 2007; *Mulitza et al.*, 2008; *Itambi et al.*, 2009]. However, the drying trend deduced from decreasing Al/Si during MIS 3 and especially during the LGM is not expressed in the grain-size data. On the other hand, drier conditions during HS 1 are indicated by extremes in Fe/K, Ti/Fe, and a coarser grain size. The double-peak of the element ratios is not clearly expressed in the grain-size data. During MIS 1, the decrease in Fe/K corresponds to a fining in the physical grain sizes.

3.4. End-Member Unmixing

[29] Contrasting patterns in the proxy records emphasize that factors influencing sediment elemental composition and grain size are diverse. Joint analyses have a potential to deliver more information about these individual factors. We suggest that both source area variability and changes in transport processes are reflected in contrasting patterns. To evaluate their relationships further, we apply an EM unmixing approach to the different parameter sets. The EM unmixing results of the grain-size and elemental data will be presented in this study, while the EM analysis of IRM acquisition curves (see Figure 5f) is reported by *Just et al.* [2012].

3.4.1. Element End-Members

[30] The element EM analysis shows an excellent fit (R^2 = 0.99 from the PCA, Figure 4) with only two EMs ($\boldsymbol{S1}_E$ and $\boldsymbol{S2}_E$, the index $\boldsymbol{E}$ denotes elemental data). Their relative element contents were transformed into elemental ratios (Table 2, part a, and Figure 5b). The contrasts in the element ratios of $\boldsymbol{S1}_E$ and $\boldsymbol{S2}_E$ resemble contrasts in the

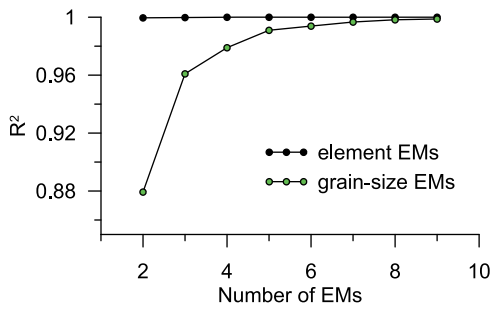

Figure 4. Coefficients of determination (R^2) obtained by principal component analyses as a decision criterion for the number of end-members used for the unmixing approach of the element and grain-size data.

Table 2. (a) Calculated Elemental Composition and Element Ratios of Element EMs (S_E) and (b) Predicted Associated Properties (P_E) of the Grain-Size End-Members

		Al	Si	K	Ti	Fe	Mg	Al/Si	Fe/K	Ti/Al	Ti/Fe
a)	$S1_E$	0.174	0.700	0.030	0.013	0.056	0.027	0.249	1.843	0.076	0.238
	$S2_E$	0.249	0.554	0.027	0.018	0.122	0.030	0.450	4.506	0.070	0.144
b)	$P1_E$	0.170	0.728	0.027	0.013	0.041	0.021	0.233	1.542	0.074	0.306
	$P2_E$	0.230	0.586	0.028	0.017	0.110	0.029	0.392	3.935	0.074	0.154
	$P3_E$	0.250	0.552	0.028	0.017	0.119	0.033	0.453	4.229	0.068	0.143

geochemical composition of present-day dust and suspension load samples of the Senegal River (cf., Table 1).

[31] The end of MIS 5, and MIS 3 and 1 are dominated by $S2_E$ (Figure 5a), while MIS 4 and 2 are dominated by $S1_E$. A gradual increase of $S1_E$ contribution is apparent throughout MIS 3 until MIS 2. Occasional increases in $S1_E$ coincide with HSs and the YD, of which HS 1 is the most pronounced. The double-peak formerly observed in the downcore element ratios, is present, but less well expressed in the EM contributions.

3.4.2. Grain-Size End-Members

[32] For the EM analysis of the granulometric data, a three EM solution appears to be optimal ($R^2 = 0.96$, Figure 4). The obtained grain-size end-members are referred to as $S1_G$, $S2_G$ and $S3_G$ (Figures 5c and 5d). $S1_G$ and $S2_G$ have clear unimodal distributions, with modes of 10 and 40 μm,

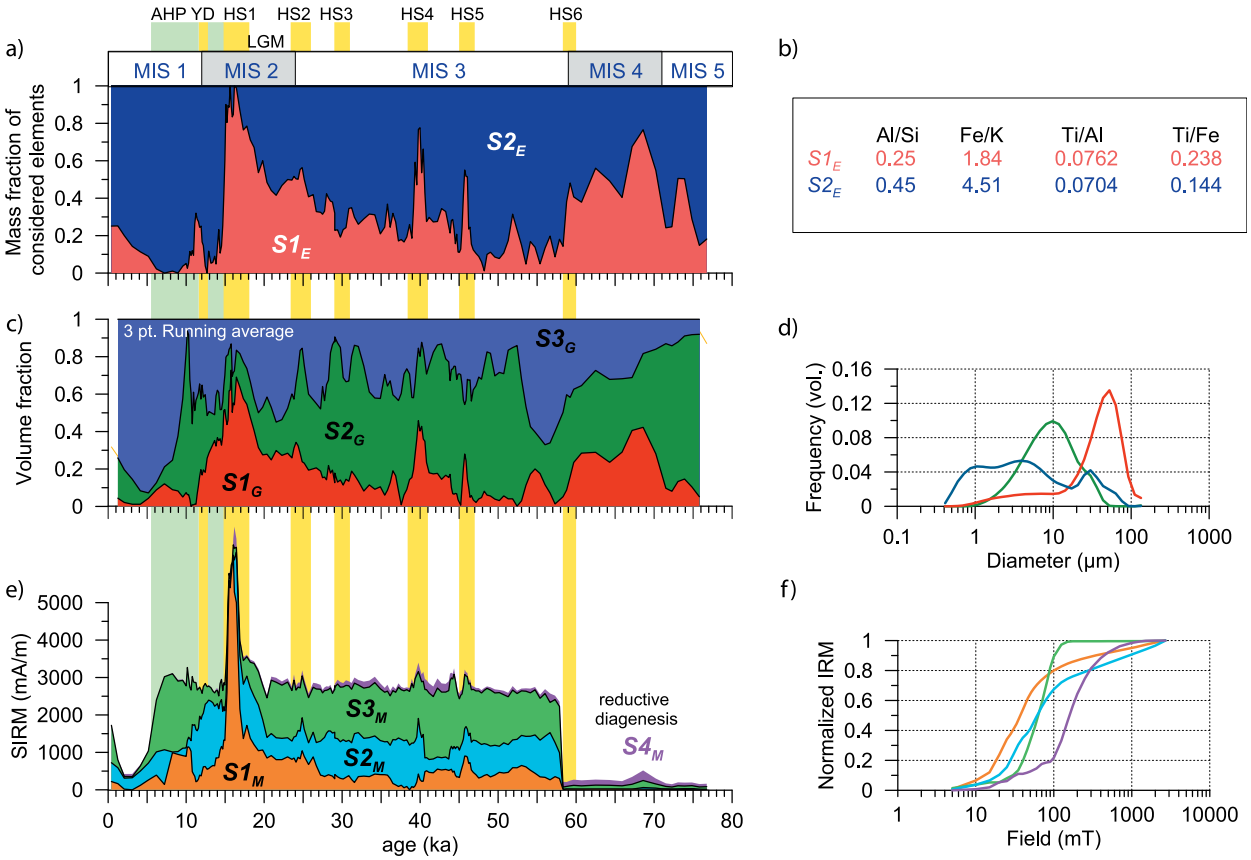

Figure 5. End-member models of the element, grain-size and rock-magnetic data. (a) Cumulative downcore contribution of element EMs (S_E). (b) Elemental ratios calculated based on the elemental composition of the EMs (cf. Table 2, part a). (c) Cumulative downcore contribution of grain-size EMs S_G. (d) Grain-size distributions of $S1_G$–$S3_G$. (e) Cumulative downcore contributions of the aeolian and fluvial magnetic S_M [*Just et al.*, 2012]. (f) The IRM acquisition curves are indicative of the magnetic mineralogy of the aeolian $S1_M$ and fluvial $S2_M$. $S3_M$ corresponds to bacterial magnetite and $S4_M$ represents a relict phase of magnetic minerals after reductive diagenesis.

respectively, while $S3_G$ has a broad distribution (1–4 μm) and small peak around 20 μm. Inclusion of an additional EM would split the medium grained $S2_G$ (10 μm) into two EMs with higher (14 μm) and lower (6 μm) modes and closely covarying contributions (data not shown). This bears a risk of over interpretation of the data, therefore this EM solution (and those with higher number of EMs) was not considered. Typically, aeolian material is coarser than fluvial material off NW Africa [*Koopmann*, 1981]. This hints to aeolian transport for the coarse $S1_G$ and fluvial transport for the fine $S3_G$. The transport pathway of $S2_G$, however, cannot be inferred at this point.

[33] $S2_G$ and $S3_G$ are generally anticorrelated, with a higher contribution of $S2_G$ except during the LGM and the late Holocene. The contribution of $S1_G$ is generally low; but increasing abundance from 50 ka until HS 1 is observed. Peaks in $S1_G$ occur during HS 5, 4, 2 and 1. HS 1 is associated with a very high contributions of $S1_G$, forming a double-peak.

3.4.3. Comparison of the End-Member Models and Relation to Rock-Magnetic End-Members

[34] The comparison of the abundances of the individual EM unmixing reveals that $S1_G$ and $S1_E$ peak during HSs. The rock-magnetic EM analysis of GeoB13602–1 reveals that four EMs are needed to unmix the IRM acquisition curve data set [*Just et al.*, 2012]. $S1_M$ corresponds to aeolian material and, from its calculated IRM acquisition curve, is characterized by a higher hematite/goethite ratio and a higher concentration of magnetite with respect to fluvial EM $S2_M$ (Figure 5f). $S3_M$ represents bacterial magnetite which was formed in situ and $S4_M$ corresponds to a magnetic relict phase due to reductive dissolution in the lower part of the core, and within a near-surface layer [*Just et al.*, 2012]. For further details about the EM characteristics we refer the reader to *Just et al.* [2012]. Their aeolian EM $S1_M$ peaks during HS 4, the LGM and has its maximum during HS 1 (Figure 5e). This co-variation is in line with the inferred aeolian nature of $S1_G$ and $S1_E$ as suggested by grain-size distributions and elemental ratios and the interpretation for the analogous rock-magnetic end-member $S1_M$ of *Just et al.* [2012].

4. Multiproxy Approach

[35] The modeled abundances of the EMs estimate the mixing proportions with respect to the input data (Figure 6): Grain-size EMs correspond to volume fractions, element EMs relate to mass fractions with regard to the total mass of the elements considered and rock magnetic EMs relate to saturation isothermal remanent magnetization (SIRM [*Just et al.*, 2012]) of each EM. Because the content of magnetic minerals within terrigenous sediments from different sources may differ, recalibrations are needed to transfer the IRM intensities into volume and mass percentages of the respective terrigenous fractions they are associated with. Calibration factors depend on the concentration of magnetic minerals within a certain volume (or mass) of bulk material and on the magnetic mineral assemblage, since magnetic minerals have different SIRMs [*Peters and Dekkers*, 2003].

[36] The grain-size EM analysis indicates that three energetic regimes exist for the transport of terrigenous sediments. It can be assumed that the different kinds of sediment properties are associated to each other, i.e., a grain-size class which is transported by a certain mechanism mirrors the distinct geochemistry and the magnetic mineralogy of the soils in the source area or experiences similar gravitational sorting processes. Therefore proportional differences between the grain-size EM fractions should be reflected in compositional differences of elements and magnetic minerals, respectively.

[37] From this assumption we developed a new approach for finding multiproxy properties of a generalized EM system. We use volumetric grain-size EM abundances $\boldsymbol{A_G}$ to predict geochemical, $\boldsymbol{P_E}$, and rock magnetic properties, $\boldsymbol{P_M}$ that are associated to the grain-size EM properties ($\boldsymbol{S_G}$). Formally

$$\boldsymbol{X_E} = \boldsymbol{A_G P_E} + \boldsymbol{R} = \widehat{\boldsymbol{X}}_{\boldsymbol{E}} + \boldsymbol{E_E} \tag{3}$$

and

$$\boldsymbol{X_M} = \boldsymbol{A_G P_M} + \boldsymbol{R} = \widehat{\boldsymbol{X}}_{\boldsymbol{M}} + \boldsymbol{E_M} \tag{4}$$

are equivalent EM mixing formulations of equation (2). $\boldsymbol{E_E}$ and $\boldsymbol{E_M}$ are matrices of residuals for the element and magnetic data sets, respectively.

[38] Since there is only one unknown, this linear problem can be solved using nonnegative least squares fitting (NNLSQ [*Löfberg*, 2004]), which respects the non-negativity constraint $\boldsymbol{P} \geq 0$. Since the element abundances are scaled to a sum of 1, the cumulative element abundances of the associated properties $\boldsymbol{P_E}$ must also be constrained to add up to 1.

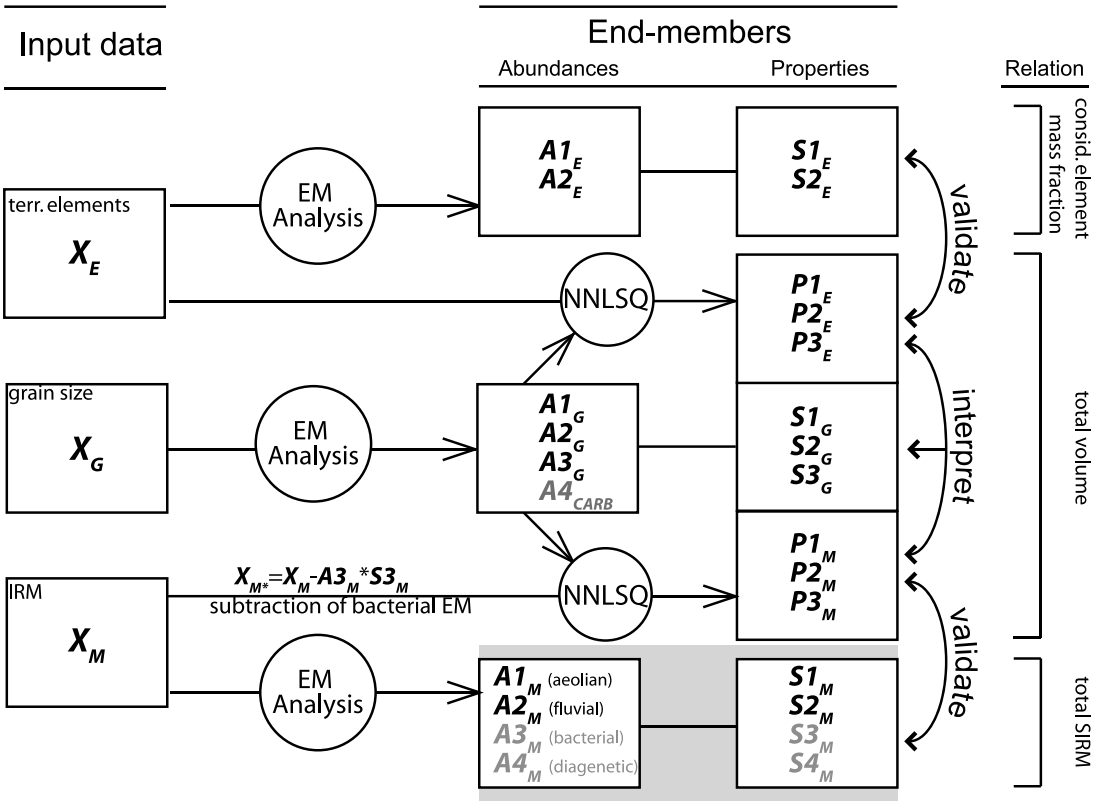

Figure 6. Schematic overview of the multiproxy EM approach. Each individual data set was unmixed using the EM unmixing algorithm of *Heslop and Dillon* [2007] yielding relative abundances $\boldsymbol{A}$ and properties $\boldsymbol{S}$. The grain-size EM contributions $\boldsymbol{A_G}$ were successively used to calculate associated geochemical ($\boldsymbol{P_E}$) and rock-magnetic properties ($\boldsymbol{P_M}$) by nonnegative least squares (NNLSQ) fitting. The obtained $\boldsymbol{P_E}$ and $\boldsymbol{P_M}$ have identical volume contributions as the $\boldsymbol{S_G}$ and are helpful to interpret the nature of the EMs. The comparison of $\boldsymbol{S_M}$ and $\boldsymbol{P_M}$ and $\boldsymbol{S_E}$ and $\boldsymbol{P_E}$ may be used to verify if changes in methodologically different EM analyses lead to consistent solutions (multiproxy validation). For the magnetic data, the contribution of the bacterial magnetite identified by *Just et al.* [2012] and carbonate ($\boldsymbol{A_C}$) content was corrected for (see text).

[39] In order to apply this approach to the IRM data, some pre-processing had to be performed. It was previously shown that one of the magnetic EMs ($\boldsymbol{S3_M}$) corresponds to biogenic magnetite [*Just et al.*, 2012] which is formed in situ and hence is not representing any terrigenous fraction. We multiplied the IRM acquisition curve of the bacterial $\boldsymbol{S3_M}$ (Figure 5f) by its contribution to SIRM of each sample ($\boldsymbol{A3_M}$, Figure 5e) and subtracted this data matrix from the original IRM acquisition curves (Figure 6).

[40] After the pre-processing the residual IRM acquisition curves should only represent the terrigenous magnetic inventory. IRM was measured on the bulk sediment, which consists of mixed terrigenous and biogenic material (mainly carbonate), which does not have an IRM. In contrast, grain-size data were analyzed on a carbonate-free basis by dissolving the carbonate prior to the grain-size analyses. To predict magnetic properties (i.e., IRM acquisition curves) from the volumetric mixing proportions of the grain-size EMs, their proportions must therefore be corrected for the missing volume of carbonate $\boldsymbol{A_C}$ (Figure 6). The volume of carbonate $\boldsymbol{A_C}$ was calculated by multiplying the mass concentration of carbonate (auxiliary material) by the dry bulk density.

[41] Additionally, we excluded the top interval and the lower part of the core where substantial reductive diagenesis has modified the magnetic mineralogy [*Just et al.*, 2012].

[42] To assess the quality of the multiproxy model, the correlation between the input data, $\boldsymbol{X}$, and the estimates, $\widehat{\boldsymbol{X}}$, derived by NNLSQ was calculated. In the case of the IRM data set, which is non-normalized and thus free of a sum-to-one constraint, the Pearson product-moment correlation coefficient

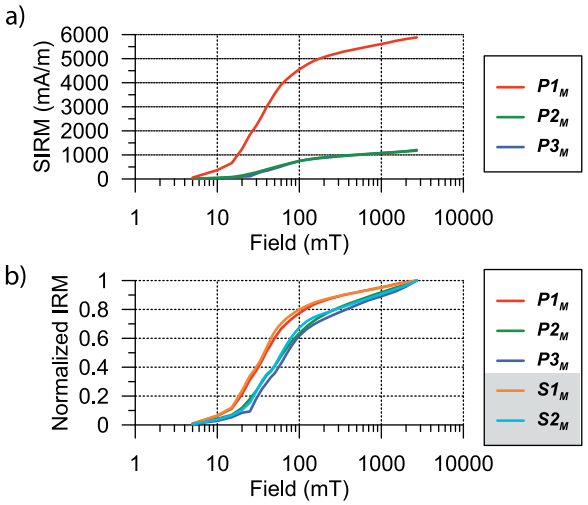

Figure 7. (a) IRM acquisition curves of $\boldsymbol{P_M}$ obtained by the least squares fitting approach. $\boldsymbol{P1_M}$ has a much higher SIRM than $\boldsymbol{P2_M}$ and $\boldsymbol{P3_M}$. (b) Normalized IRM curves $\boldsymbol{P_M}$ in comparison to $\boldsymbol{S_M}$ obtained by unmixing the IRM data [*Just et al.*, 2012]. The strong similarity indicates that the mixing proportions of grain-size end-member $\boldsymbol{S_G}$ can be equally used for unmixing the IRM acquisitions curves, as the mixing proportions obtained by IRM end-member analysis (see Figure 5).

was calculated. For the compositional data set of element relative abundances we performed the centered-log-ratio transformation [*Aitchison*, 1982] to bring the data $\boldsymbol{X_E}$ and estimates $\widehat{\boldsymbol{X}}_{\boldsymbol{E}}$ into real space. Afterwards a correlation coefficient analogous to the Pearson product-moment correlation coefficient for compositional data was calculated. In both cases the significance of the correlation was assessed using a *Monte Carlo* randomization test with 10^4 iterations. For $\widehat{\boldsymbol{X}}$ and $\boldsymbol{X_M}$ the coefficient of determination is 0.51 (corresponding to a significance level of <0.0001). When comparing $\boldsymbol{X_E}$ and $\widehat{\boldsymbol{X}}_{\boldsymbol{E}}$ the calculated squared correlation is 0.63 (significant at a level of <0.0001).

4.1. Multiproxy Properties

[43] The elemental ratios $\boldsymbol{P_E}$ associated to the grain-size EMs are given in Table 2, part b. A striking feature is that the associated elemental composition $\boldsymbol{P1_E}$ of the coarse grain-size EM $\boldsymbol{S1_G}$ is distinctly different from $\boldsymbol{P2_E}$ and $\boldsymbol{P3_E}$. $\boldsymbol{P1_E}$ has low Al/Si and Fe/K and high Ti/Fe ratios while both fine-grained EMs are associated to high Al/Si and Fe/K and low Ti/Fe ratios.

[44] Likewise, the IRM acquisition curve of $\boldsymbol{P1_M}$ is distinctively different from $\boldsymbol{P2_M}$ and $\boldsymbol{P3_M}$ (Figure 7a), while the latter two curves are very similar. To compare the shape of the curves, which is indicative of the magnetic mineralogy, we normalized them to one (Figure 7b). Again, the shape of $\boldsymbol{P1_M}$ is distinctively different; the slope starts to rise at lower fields and is flatter at high fields compared to $\boldsymbol{P2_M}$ and $\boldsymbol{P3_M}$. This indicates that $\boldsymbol{P1_M}$ contains a higher proportion of magnetite and higher hematite/goethite, compared to $\boldsymbol{P2_M}$ and $\boldsymbol{P3_M}$. A comparison of the associated properties of the grain-size EMs with the EMs obtained by direct unmixing of the magnetic and geochemical data reveals large similarities between both solutions (Figure 7b and Table 2, parts a and b) and can be used to verify each solution (Figure 6).

5. Discussion

5.1. Multiproxy Properties of Terrigenous End-Members

[45] Since the associated properties of the grain-size EMs appear to provide a good representation of the EMs of the individual analysis, we can elucidate the nature of the grain-size EMs from a geochemical and rock-magnetic perspective. The coarse mode of $\boldsymbol{S1_G}$ is in the range of typical grain sizes (8–42 μm) for dust collected off NW Africa [*Stuut et al.*, 2005]. The associated geochemical properties $\boldsymbol{P1_E}$ (Table 2) are similar to aeolian deposits in SW Niger [*Moreno et al.*, 2006] and low Fe/K ratio of present-day dust samples collected at Sal Island [*Chiapello et al.*, 1997] (Table 1). However, the Al/Si ratio of the Sal Island samples is significantly higher, than in $\boldsymbol{P1_E}$. This phenomenon is most likely attributed to gravitational sorting during transport, suggesting a shorter distance between our core location and the dust source compared to the deposits from Sal Island. This interpretation is in line with the coarse grain-size distribution $\boldsymbol{S1_G}$. Further, the normalized IRM acquisition curve $\boldsymbol{P1_M}$ resembles the IRM acquisition curve of $\boldsymbol{S1_M}$ which has been identified as an aeolian EM [*Just et al.*, 2012] with a magnetic inventory containing a high concentration of magnetite and a high hematite/goethite ratio.

[46] According to their associated properties, the medium (10 μm) and fine grained EMs (1–4 μm) have similar elemental compositions and magnetic mineralogies, which yields several clues for their interpretation: (a) The present-day suspension load at the mouth of the Gambia river consists of grains finer than 10 μm [*Gac and Kane*, 1986, and references therein]. (b) The elemental ratios $\boldsymbol{P2_E}$ and $\boldsymbol{P3_E}$ resemble fluvial samples of the suspension

load of the Senegal river [*Gac and Kane*, 1986] (Table 1). (c) The IRM acquisition curves $\boldsymbol{P2_M}$ and $\boldsymbol{P3_M}$ are similar to $\boldsymbol{S2_M}$ which was interpreted as a fluvial EM with a lower hematite/goethite ratio and a lower relative concentration of magnetite [*Just et al.*, 2012].

[47] The similar elemental compositions and magnetic mineralogies demonstrate that both EMs correspond to sediments that originate from the same source area (i.e., Gambia River catchment), but are transported under different energetic conditions. Since the Gambia River drainage basin is relatively well vegetated, its potential for aeolian deflation of material is low and thus both the medium- and fine-grained EMs must have been transported by the Gambia River. The medium grained EM (10 μm) falls into the range of present-day dust collected off NW Africa [*Stuut et al.*, 2005] and might therefore correspond to a mixture of aeolian and fluvial material. However, given the strong similarity of elemental ratios ($\boldsymbol{P2_E}$) and magnetic mineralogy ($\boldsymbol{P2_M}$) to the fine grained EM ($\boldsymbol{P3_E}$, $\boldsymbol{P3_M}$), the medium grained EM must be dominated by fluvial sediments and the bias introduced by aeolian material must be small.

[48] Only the joint characterization of the multiparameter properties enables the identification of the medium grained EM $\boldsymbol{S2_G}$ as a fluvial EM. By their very nature, magnetic and geochemical data are more indicative for source area characteristics, while grain size is primarily controlled by transport conditions. We will further discuss differences in the grain-size distribution of the fluvial EMs in section 5.3.

5.2. Budgeting the Accumulation of Terrigenous End-Members

[49] Because only the grain-size EM system represents volumetric contribution of aeolian and fluvial fractions, we used the grain-size EM contributions to quantify the fluxes of terrigenous sediments to the continental margin off Gambia.

[50] The total MARs in core GeoB 13602–1 vary between 30 g m^{-2} yr^{-1} and 700 g m^{-2} yr^{-1} (Figure 8e). Note that in the lowest part of the core (MIS 5 and 4) the mass accumulation rates are probably underestimated because squeezing out of sediments during gravity coring is likely [*Just et al.*, 2012]. The accumulation of the fluvial EMs (Figure 8e) is on average higher than that of the aeolian EM with a few exceptions during HSs and the LGM. This is in accordance with the calculations of *Collins et al.* [2011] who investigated the dust/river ratio in sediment cores of a transect from 21°N to 23°S off W Africa. At 12°N, they found a dust/river proportion of ~0.3 in the Holocene and ratios of ~1.2 and ~2.5 during the LGM and HS 1, respectively. Our analysis reveals a similar pattern. However, it seems that also during HSs the accumulation of fluvial material increases. This pattern is most probably an artifact of the age model because of the short-term character of HSs and their extremely high accumulation rates. The lack of age-control points leads to blurring of fluvial accumulation rates before and after the punctured peaks of high dust input.

[51] However, since fluvial sediment accumulation did not completely diminish during HSs we suggest that reported dry conditions only affected the source areas of aeolian material (i.e., their areal extent) but seem to have had little influence on rainfall in the Gambia River catchment and respectively the fluvial discharge of suspended material.

[52] Exceptionally high MARs during HS 1 show massive levels of aeolian input. The deglaciation until ~10 ka is marked by high accumulation rates of fluvial material in the range of 100 to 300 g m^{-2} yr^{-1}. Subsequently, MARs of the fluvial EMs are reduced to 40 g m^{-2} yr^{-1} while the accumulation of aeolian material diminishes to less than 10 g m^{-2} yr^{-1}. This dust accumulation rate during the Holocene is in good accordance with other studies in the region [*Kohfeld and Harrison*, 2001] and estimates obtained by numerical modeling [*Mahowald et al.*, 2006].

[53] Difficulties arise when comparing absolute dust accumulation rates from different sites, since the deposition is influenced by regional conditions i.e., the presence of potential dust sources in the hinterland and the source-to-sink distance. To compare flux changes at different sites, it is useful to normalize the dust input to a site specific reference. The data compilation in the DIRTMAP project [*Kohfeld and Harrison*, 2001] uses the modern dust accumulation at each site as a reference. Accordingly, we use the calculated dust accumulation at GeoB 13602–1 during the Late Holocene as a reference to express the proportion of dust throughout our record and the Holocene as the aeolian accumulation index (AAI, Figures 8f and 9). The averaged accumulation rates of aeolian material in GeoB 13602–1 during MIS 3 and the LGM correspond to AAIs of 3 and 7, respectively. The value for the LGM is in the order of the dust deposition estimates for our study area during the LGM obtained from numerical

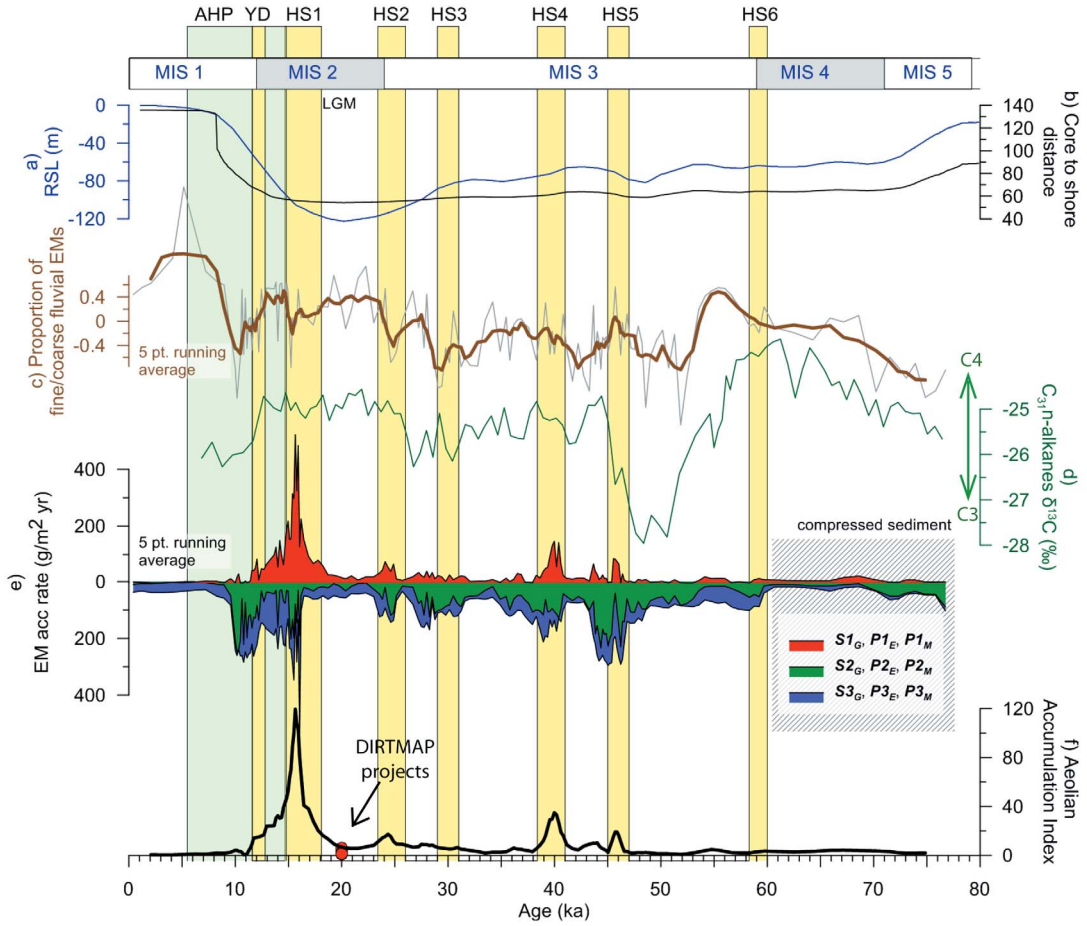

Figure 8. (a) Relative sea level (RSL) curve adopted from *Waelbroeck et al.* [2002] and (b) corresponding distance of the study site to the shoreline calculated based on the bathymetry of the shelf (extracted from GEBCO data). (c) Log ratio of the fine-grained to the coarse-grained EM (gray) and 5 point running average (brown line). (d) $\delta^{13}C$ of long chained *n*-alkanes of GeoB 9528–3 [*Castañeda et al.*, 2009]. Lower values correspond to phases with a higher proportion of C3 plants (trees) with respect to C4 plants (grasses). (e) Mass accumulation rates derived from the grain-size EM analysis. (f) The aeolian accumulation index (AAI) corresponds to the past dust accumulation in GeoB 13602–1 normalized to the Late Holocene dust accumulation at the respective site. The red points correspond to AAIs of the DIRTMAP project compilation [*Kohfeld and Harrison*, 2001], see also Figure 9.

modeling [*Mahowald et al.*, 2006]. Studies compiled in the DIRTMAP project [*Kohfeld and Harrison*, 2001] report AAIs of 1.5–6 during the LGM (Figures 8f and 9).

[54] According to the GeoB 13602–1 record, far higher dust fluxes (AAIs of 8–35) were reached during HS 5, HS 4 and HS 2. The highest accumulation of aeolian materials occurred during HS 1 and is in the order of 300 g m^{-2} yr^{-1} (mean AAI 80). Note that this AAI is at least 10 times higher than during the LGM. This finding emphasizes that short-term disturbances of the meridional overturning circulation have a major impact also on low latitudes climate (cf. section 5.3.2) and particularly on dust fluxes.

5.3. Source Areas and Transport Processes

5.3.1. Fluvial Material

[55] Generally, two factors control the accumulation and the grain-size distribution of fluvial material at continental margins: (1) the transport distance (i.e., coarse-grained sediments will be deposited in the proximity of the river mouth) and (2) the extent of the suspension plume (potential for sediment transport out at sea). The latter is influenced by the river flow velocity and the water discharge, i.e., precipitation in the hinterland [*Zabel et al.*, 2001]. Additionally, varying ocean current velocities may lead to a displacement of the deposition zone of a certain grain-size class. Without detailed paleocurrent

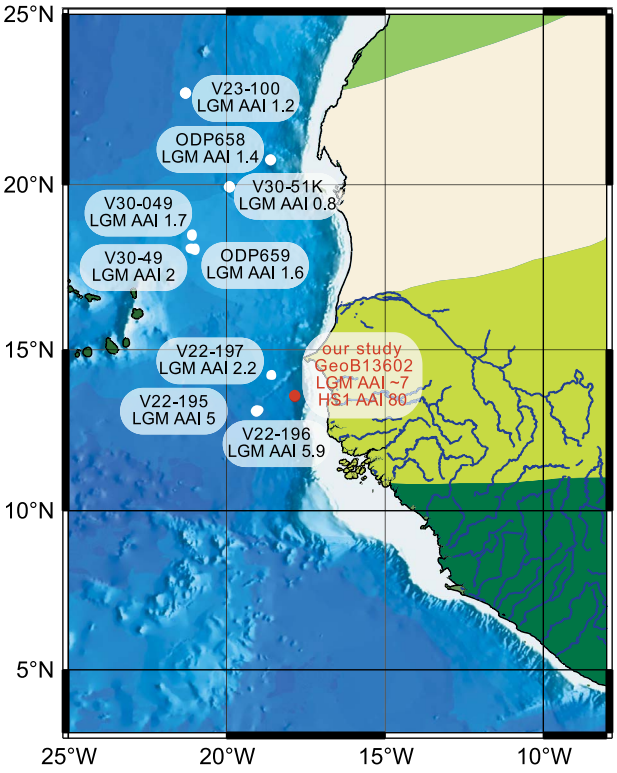

Figure 9. Aeolian accumulation index (AAI) from different sites off NW Africa [*Kohfeld and Harrison*, 2001]. Data are only available for the LGM (Last Glacial Maximum). Note that AAI at our study site is in the same order as AAIs reported in the literature but is at least 10 times lower than the AAI for HS 1.

reconstructions, the latter effect is hard to quantify. Numerical modeling approaches indicate that the net N-S horizontal volume transport in the eastern Atlantic Ocean did not differ substantially during the LGM [*Schäfer-Neth and Paul*, 2004]. However, the stratification and depth of oceanographic boundary layers were different; a shallowing of northern sourced waters and ingression of SACW is evident [*Sarnthein et al.*, 1994; *Bickert and Mackensen*, 2004; *Lynch-Stieglitz et al.*, 2007]. To the best of our knowledge there are no regional paleocurrent reconstructions which integrate over the entire water column and could be indicative for a change in the deposition center of suspended or advected material in our study area. Therefore we assume that the integrated net transport of suspended material did not vary significantly during the last glacial on a regional scale and is essentially the same as today. We focus here on the potential effects of transport distance (i.e., distance from the core location to the river mouth) and transport energy.

[56] During MIS 4 and MIS 3 sea level was 60–80 m lower than today [*Waelbroeck et al.*, 2002] and reached its lowest position during MIS 2 (LGM, Figure 8a). Accordingly, the distance from the core location to the river mouth reached a minimum. Due to the morphology of the flat-topped shelf, the core-to-shore distance remained relatively stable (~55 km) once sea level fall reached a threshold of ~60 m (Figure 8b). A major transgression occurred during the deglaciation which ended at 8 ka, resulting in the present-day core-to-shore distance of ~140 km.

[57] The sea-level fall and rise during MIS 5 and MIS 1, respectively, and the related distance-to-shore curve, coincide roughly with total accumulation of fluvial material (Figure 8e), indicating that the distance from the river mouth to the study site plays an important role. However, the proportion of fine- and coarse-grained fluvial sediments especially during MIS 4, 3 and 2 cannot be explained by sea-level variations alone.

[58] It can be hypothesized that during humid periods, and thus times of higher water discharge, the fan of suspended material was more extensive and thus coarse particles were transported farther out at sea, leading to a coarsening of the fluvial deposits and to a lowering of the dust/river proportion. To consider the transport energy of the river, i.e., the water discharge, we investigate published proxy studies focusing on precipitation on the continent itself and compare them to the ratio between the fine- and coarse-grained fluvial EM fractions (Figure 8c). *Castañeda et al.* [2009] measured the $\delta^{13}C$ of long-chained *n*-alkanes (Figure 8d) on sediment core GeoB 9528–3 (09°09.96N, 17°39.81W, Figure 1). These plant waxes are contained in aeolian material of which the source area is assumed to be at the Sahara-Sahel boundary [*Castañeda et al.*, 2009]. The variations in $\delta^{13}C$ can be regarded as a proxy for the relative proportions of C_4 (grasses) and C_3 plants (trees, shrubs), of which occurrence in NW Africa depends on humidity [*Castañeda et al.*, 2009, and references therein]. A relative increase in C_4 vegetation at the end of MIS 5 and MIS 4 (Figure 8d) indicates drying conditions while increasing humidity (relative increase of C_3 plants) occurs at the beginning of MIS 3 (50–45) ka.

[59] The aridification during MIS 5 and MIS 4 is expressed by a relative decrease in fluvial input with respect to the aeolian fraction. During MIS 3, the strong relative increase in C_3 vegetation is roughly correlated to an increase of the fine/coarse

fluvial EM ratio (Figure 8c). However, the prominent peak in C_3 vegetation around 50 ka has no counterpart in the coarse fluvial EM. In the beginning of MIS 2, the proportion of fine/coarse fluvial EMs increases, which might point to lower water discharge of the Gambia River in line with drier conditions, i.e., less precipitation, suggested by increased C_4 proportion [*Castañeda et al.*, 2009] and modeling approaches [*Van Meerbeeck et al.*, 2008]. Similarly, a record of δD ratios of n-alkanes in a sediment core off the Senegal River indicates decreasing rainfall at the MIS 3/2 transition [*Niedermeyer et al.*, 2010].

[60] During more humid last deglacial conditions the fraction of the coarse fluvial EM ($\boldsymbol{S2_G}$) is again enhanced. During the Mid-Holocene AHP [*deMenocal et al.*, 2000b] - which has been ascribed the most humid period during the entire Holocene in sub-tropical and arid NW Africa [*deMenocal et al.*, 2000b; *Collins et al.*, 2011; *Meyer et al.*, 2011] - the fine fluvial EM is re-established, which seems to be in conflict with the relationship outlined above. However, this period corresponds to the time of major sea-level rise, and thus a dramatic increase of the distance between core location and river mouth. This sea-level effect is apparently more important for the deposition of fluvial materials than higher precipitation.

[61] Significant drops in the proportion of fine to coarse fluvial EMs mark HS 2 and 3, which is rather unexpected, given the consideration of a higher proportion of fine/coarse fluvial material during arid than during humid conditions. We suppose that this peak corresponds to a non-perfect unmixing of fluvial and aeolian material for HS 2; relatively fine-grained dust is mingled with the coarse-grained fluvial EM. Since the input of aeolian material appears to be rather low during HS 3 (see Figures 8e and 8f), we infer that the pattern during HS 3 is not associated with the same unmixing error. Also, for HS 1, 4 and 5 no significant minima are observed. We thus conclude that the unmixing procedure worked properly for most of the record and aeolian material is mainly represented by $\boldsymbol{S1_G}$ (cf. section 5.1).

5.3.2. Aeolian Material

[62] The accumulation of aeolian material is controlled by wind strength, frequency of dust outbreaks, source-to-sink distance, and areal extent of dust sources. The latter is dependent on vegetation cover in the hinterland, primarily a function of precipitation. Widely exposed shelf areas may be subject to deflation under dry conditions and act as additional sources, especially during times of low sea level. The high dust flux during MIS 3, MIS 2 and particularly during HS 1 (Figures 8e and 8f) implies very different environmental conditions in NW Africa during those periods. The recognizable correlation between vegetation cover and proportion of aeolian material, especially at the MIS 3/2 transition, indicates that the expansion and contraction of the desert is the main driving mechanism for dust export from the continent. The rising sea level during the last deglaciation coincides with a decrease in dust contribution pointing to the influence of exposed shelves and regional dust sources during MIS 4 to MIS 2. Southward advancing dune fields [*Maley*, 2000] during the LGM could also have constituted additional dust sources. However, our approach reveals that the magnetic mineralogy and geochemical composition of dust did not vary. It may therefore be inferred that regional remobilized sediments correspond to deposits originating from the Sahara. Since the most extensive exposed shelves existed during the LGM, the high dust accumulation during HS 1 cannot solely be attributed to desiccated shelf-areas and should rather result from southerly expanded deserts.

[63] It has been suggested that during the LGM the Trades were much stronger compared to present-day [*Hooghiemstra et al.*, 2006, and references therein] and that the zonal wind field (AEJ) was also enhanced during Heinrich Stadials [*Mulitza et al.*, 2008]. This should affect the accumulation of the aeolian fraction and its grain size. Since only one EM is resolved in our study, the inferred coarsening is not apparent in our EM unmixing. Since the grain-size spectrum of the aeolian EM integrates over a certain grain-size range, it remains questionable, whether EM modeling is capable of detecting changes in wind strength, at least with the present input parameters.

[64] Our data suggests that dust events were more frequent (i.e., longer 'dusty' seasons during HS 1) and dust sources were larger. Likewise, *Collins et al.* [2011] inferred a shorter wet season for the LGM and HS 1 from vegetation proxies. The double peak observed in the proxy data and EM models indicates that during HS 1, environmental conditions may have changed rapidly. Higher resolution records are needed to understand if such changes during HS 1 are associated to separate North Atlantic freshwater injections features, i.e., precursors of iceberg discharge in advance of Heinrich

Events [e.g., *Grousset et al.*, 2001; *Jullien et al.*, 2007].

6. Conclusion

[65] A combined strategy of end-member analysis and least squares-fitting techniques enabled us to determine volume calibrated multiparameter properties for each identified EM. Geochemical element and rock magnetic EM abundances correspond to total mass or saturation remanence contributions, respectively, but are not intrinsically volume calibrated. NNLSQ fitting of the volumetric grain-size EM contributions with the geochemical and rock-magnetic sample properties provides such a volume calibration.

[66] While only two magnetic or two element EMs suffice to unmix the terrigenous sediment fraction of core GeoB 13602–1, three grain-size EMs were required to fit all observed grain-size distributions. The associated EM properties reveal that the fine (<4 μm) and medium (mode 10 μm) grain-size EMs have very similar magnetic and geochemical signatures indicative of fluvial sediments in sub-tropical Africa. A coarse grain-size aeolian EM (mode 40 μm) has a contrasting composition marked by lower Al/Si and Fe/K and higher Ti/Fe ratios, consistent with earlier dust studies, as well as a higher hematite to goethite ratio in line with soil formation under more arid climates.

[67] In combination, the granulometric, geochemical and rock-magnetic characteristics enable univocal interpretations and validations of all single-parameter EMs: Grain-sizes can discriminate fluvial and aeolian fractions only if transport energies differ significantly. Geochemical composition and the magnetic mineralogy are distinctive, if sediments originate from petrologically and/or pedogenically contrasting sources. After the identification of aeolian and fluvial EMs by their multiproperty characteristics, their volume fractions permit their individual accumulation rates to be budgeted.

[68] At our core position, fluvial sediment accumulation is generally higher than dust deposition, although, during HSs and the LGM the ratio of aeolian/fluvial material can reach ~1. The accumulation and grain-sizes of the fluvial fraction are primarily controlled by the distance between river mouth and core location, i.e., sea level variations, and secondarily by precipitation in the hinterland.

[69] According to our analysis, the flux of aeolian material during the LGM was 7 times higher than today, but not higher than during MIS 3–4. The most extreme dust input (~300 g m^{-2} yr^{-1}) occurred during HS 1, 80 times higher compared to modern times. The driving factor for dust accumulation is the presence of freshly exposed or desiccated source areas for deflation. Exposed shelves may have served as additional dust sources but only a rapid vegetation retreat can explain the observed fluxes during HSs. The fluvial input does not appear to be significantly reduced during HSs, suggesting that aridification during HSs did not reach the catchment region of the Gambia River.

Acknowledgments

[70] We thank the crew and scientific party of *Maria S. Merian* cruise MSM 11/2 for helping to collect the studied cores. We acknowledge the helpful comments of three anonymous reviewers. This study was funded by the Deutsche Forschungsgemeinschaft (DFG) through the international graduate college EUROPROX- Proxies in Earth History and through DFG-Research Center / Cluster of Excellence "The Ocean in the Earth System" MARUM – Center for Marine Environmental Sciences. DH was supported by the Australian Research Council (grant DP110105419). The data for this study available in the PANGAE database http://doi.pangaea.de/10.1594/PANGAEA.788181.

References

Aitchison, J. (1982), The statistical analysis of compositional data, *J. R. Stat. Soc., B*, *44*, 139–177.

Balsam, W. L., B. L. Otto-Bliesner, and B. C. Deaton (1995), Modern and Last Glacial Maximum eolian sedimentation patterns in the Atlantic Ocean interpreted from sediment iron oxide content, *Paleoceanography*, *10*(3), 493, doi:10.1029/95PA00421.

Bickert, T., and A. Mackensen (2004), Last Glacial to Holocene changes in South Atlantic deep water circulation, in *The South Atlantic in the Late Quaternary - Reconstruction of Material Budget and Current Systems*, edited by G. Wefer, S. Mulitza, and V. Ratmeyer, pp. 671–695, Springer, Berlin, doi:10.1007/978-3-642-18917-3_29.

Bouimetarhan, I., L. Dupont, E. Schefuß, G. Mollenhauer, S. Mulitza, and K. Zonneveld (2009), Palynological evidence for climatic and oceanic variability off NW Africa during the late Holocene, *Quat. Res.*, *72*, 188–197, doi:10.1016/j.yqres.2009.05.003.

Boyle, E. A. (1983), Chemical accumulation variations under the Peru Current during the past 130,000 years, *J. Geophys. Res.*, *88*, 7667–7680, doi:10.1029/JC088iC12p07667.

Castañeda, I., S. Mulitza, E. Schefuß, R. A. Lopes dos Santos, J. S. Sinninghe Damsté, and S. Schouten (2009), Wet phases in the Sahara/Sahel region and human migration patterns in North Africa, *Proc. Natl. Acad. Sci. U. S. A.*, *106*, 20,159–20,163, doi:10.1073/pnas.0905771106.

Chiapello, I., G. Bergametti, B. Chatenet, P. Bousquet, F. Dulac, and E. S. Soares (1997), Origins of African dust transported

over the northeastern tropical Atlantic, *J. Geophys. Res.*, *102*, 13,701–13,709, doi:10.1029/97JD00259.

COHMAP Members (1988), Climatic changes of the last 18,000 years: Observations and model simulations, *Science*, *241*, 1043–1052, doi:10.1126/science.241.4869.1043.

Collins, J. A., et al. (2011), Interhemispheric symmetry of the tropical African rainbelt over the past 23,000 years, *Nat. Geosci.*, *4*, 42–45, doi:10.1038/ngeo1039.

deMenocal, P., J. Ortiz, T. Guilderson, and M. Sarnthein (2000a), Coherent high- and low-latitude climate variability during the Holocene Warm Period, *Science*, *288*, 2198–2202, doi:10.1126/science.288.5474.2198.

deMenocal, P., J. Ortiz, T. Guilderson, J. Adkins, M. Sarnthein, L. Baker, and M. Yarusinsky (2000b), Abrupt onset and termination of the African Humid Period: Rapid climate responses to gradual insolation forcing, *Quat. Sci. Rev.*, *19*, 347–361, doi:10.1016/S0277-3791(99)00081-5.

Engelstaedter, S., I. Tegen, and R. Washington (2006), North African dust emissions and transport, *Earth Sci. Rev.*, *79*, 73–100, doi:10.1016/j.earscirev.2006.06.004.

FAO, IIASA, ISRIC, ISSCAS, and JRC (2009), Harmonized World Soil Database (version 1.1), software, FAO, Rome.

Gac, J. Y., and A. Kane (1986), Le fleuve Sénégal: I Bilan hydrologique et flux continentaux der matières particulaires a l'embouchure, *Sci. Geol. Bull.*, *39*, 99–130.

Gasse, F. (2000), Hydrological changes in the African tropics since the Last Glacial Maximum, *Quat. Sci. Rev.*, *19*, 189–211, doi:10.1016/S0277-3791(99)00061-X.

Gasse, F. (2001), Paleocliamte: Hydrological changes in Africa, *Science*, *292*, 2259–2260, doi:10.1126/science.1061940.

Gasse, F. (2006), Climate and hydrological changes in tropical Africa during the past million years, *C. R. Palevol*, *5*, 35–43, doi:10.1016/j.crpv.2005.09.012.

Govin, A., U. Holzwarth, D. Heslop, L. Ford Keeling, M. Zabel, S. Mulitza, J. A. Collins, and C. M. Chiessi (2012), Distribution of major elements in Atlantic surface sediments (36°N-49°S): Imprint of terrigenous input and continental weathering, *Geochem. Geophys. Geosyst.*, *13*, Q01013, doi:10.1029/2011GC003785.

Govindaraju, K. (1994), 1994 Complilation of working values and sample description for 383 geostandards, *Geostand. Newsl.*, *18*, 1–158, doi:10.1111/j.1751-908X.1994.tb00502.x.

Grousset, F. E., E. Cortijo, S. Huon, L. Hervé, T. Richter, D. Burdloff, J. Duprat, and O. Weber (2001), Zooming in on Heinrich layers, *Paleoceanography*, *16*, 240–259, doi:10.1029/2000PA000559.

Heslop, D., and M. Dillon (2007), Unmixing magnetic remanence curves without *a priori* knowledge, *Geophys. J. Int.*, *170*, 556–566, doi:10.1111/j.1365-246X.2007.03432.x.

Holz, C., J.-B. W. Stuut, R. Henrich, and H. Meggers (2007), Variability in terrigenous sedimentation processes off northwest Africa and its relation to climate changes: Inferences from grain-size distributions of a Holocene marine sediment record, *Sediment. Geol.*, *202*, 499–508, doi:10.1016/j.sedgeo.2007.03.015.

Hooghiemstra, H., A.-M. Lézine, S. A. G. Leroy, L. Dupont, and F. Marret (2006), Late Quaternary palynology in marine sediments: A synthesis of the understanding of pollen distribution patterns in the NW African setting, *Quat. Int.*, *148*, 29–44, doi:10.1016/j.quaint.2005.11.005.

Itambi, A. C., T. von Dobeneck, S. Mulitza, T. Bickert, and D. Heslop (2009), Millennial-scale northwest African droughts related to Heinrich events and Dansgaard-Oeschger cycles: Evidence in marine sediments from offshore Senegal, *Paleoceanography*, *24*, PA1205, doi:10.1029/2007PA001570.

Jullien, E., et al. (2007), Low-latitude "dusty events" vs. high-latitude "icy Heinrich events", *Quat. Res.*, *68*, 379–386, doi:10.1016/j.yqres.2007.07.007.

Just, J., M. J. Dekkers, T. von Dobeneck, A. van Hoesel, and T. Bickert (2012), Signatures and significance of aeolian, fluvial, bacterial and diagenetic magnetic mineral fractions in Late Quaternary marine sediments off Gambia, NW Africa, *Geochem. Geophys. Geosyst.*, *13*, Q0AO02, doi:10.1029/2012GC004146.

Kohfeld, K. E., and S. P. Harrison (2001), DIRTMAP: The geological record of dust, *Earth Sci. Rev.*, *54*, 81–114, doi:10.1016/S0012-8252(01)00042-3.

Koopmann, B. (1981), Sedimentation von Saharastaub im subtropischen Nordatlantik während der letzten 25.000 Jahre, *Meteor Forschungergeb.*, *35*, 23–59.

Larrasoaña, J. C., A. P. Roberts, E. J. Rohling, M. Winklhofer, and R. Wehausen (2003), Three million years of monsoon variability over the northern Sahara, *Clim. Dyn.*, *21*, 689–698, doi:10.1007/s00382-003-0355-z.

Lesack, L. F. W., R. E. Hecky, and J. M. Melack (1984), Transport of carbon, nitrogen, phosphorus, and major solutes in the Gambia River, West Africa, *Limnol. Oceanogr.*, *29*, 816–830, doi:10.4319/lo.1984.29.4.0816.

Löfberg, J. (2004), YALMIP: A toolbox for modeling and optimization in MATLAB, paper presented at CACSD Conference, Taipei, Taiwan.

Lynch-Stieglitz, J., et al. (2007), Atlantic meridional overturning circulation during the Last Glacial Maximum, *Science*, *316*, 66–69, doi:10.1126/science.1137127.

Mahowald, N., K. Kohfeld, M. Hansson, Y. Balkanski, S. P. Harrison, I. C. Prentice, M. Schulz, and H. Rodhe (1999), Dust sources and deposition during the last glacial maximum and current climate: A comparison of model results with paleodata from ice cores and marine sediments, *J. Geophys. Res.*, *104*, 15,895–15,916, doi:10.1029/1999JD900084.

Mahowald, N. M., D. R. Muhs, S. Levis, P. J. Rasch, M. Yoshioka, C. S. Zender, and C. Luo (2006), Change in atmospheric mineral aerosols in response to climate: Last glacial period, preindustrial, modern, and doubled carbon dioxide climates, *J. Geophys. Res.*, *111*, D10202, doi:10.1029/2005JD006653.

Maley, J. (2000), Last Glacial Maximum lacustrine and fluviatile formations in the Tibesti and other Saharan mountains, and large-scale climatic teleconnections linked to the activity of the Subtropical Jet Stream, *Global Planet. Change*, *26*, 121–136, doi:10.1016/S0921-8181(00)00039-4.

Matthewson, A. P., G. B. Shimmield, D. Kroon, and A. E. Fallick (1995), A 300 kyr High-Resolution Aridity Record of the North African Continent, *Paleoceanography*, *10*, 677–692, doi:10.1029/94PA03348.

Meyer, I., G. R. Davies, and J.-B. W. Stuut (2011), Grain size control on Sr-Nd isotope provenance studies and impact on paleoclimate reconstructions: An example from deep-sea sediments offshore NW Africa, *Geochem. Geophys. Geosyst.*, *12*, Q03005, doi:10.1029/2010GC003355.

Moreno, T., X. Querol, S. Castillo, A. Alastuey, E. Cuevas, L. Herrmann, M. Mounkaila, J. Elvira, and W. Gibbons (2006), Geochemical variations in aeolian mineral particles from the Sahara-Sahel Dust Corridor, *Chemosphere*, *65*, 261–270, doi:10.1016/j.chemosphere.2006.02.052.

Mulitza, S., M. Prange, J. B. Stuut, M. Zabel, T. von Dobeneck, A. C. Itambi, J. Nizou, M. Schulz, and G. Wefer (2008), Sahel megadroughts triggered by glacial slowdowns of Atlantic meridional overturning, *Paleoceanography*, *23*, PA4206, doi:10.1029/2008PA001637.

Niedermeyer, E. M., E. Schefuß, A. L. Sessions, S. Mulitza, G. Mollenhauer, M. Schulz, and G. Wefer (2010), Orbital- and millennial-scale changes in the hydrologic cycle and vegetation in the western African Sahel: Insights from individual plant wax [delta]D and [delta]13C, *Quat. Sci. Rev.*, *29*, 2996–3005, doi:10.1016/j.quascirev.2010.06.039.

Peters, C., and M. J. Dekkers (2003), Selected room temperature magnetic parameters as a function of mineralogy, concentration and grain size, *Phys. Chem. Earth, Parts A, B, and C*, *28*, 659–667, doi:10.1016/S1474-7065(03)00120-7.

Prospero, J. M. (1996), The atmospheric transport of particles to the ocean, in *Particle Flux in the Ocean*, edited by V. Ittekkott, S. Honjo, and P. J. Depetris, pp. 19–52, John Wiley, New York.

Prospero, J. M., P. Ginoux, O. Torres, S. E. Nicholson, and T. E. Gill (2002), Environmental characterization of global sources of atmospheric soil dust identified with the NIMBUS 7 Total Ozone Mapping Spectrometer (TOMS) absorbing aerosol product, *Rev. Geophys.*, *40*(1), 1002, doi:10.1029/2000RG000095.

Pye, K. (1987), *Aeolian Dust and Dust Deposits*, 334 pp., Academic, London.

Ruddiman, W. F. (1997), Tropical Atlantic terrigenous fluxes since 25,000 yrs B.P, *Mar. Geol.*, *136*, 189–207, doi:10.1016/S0025-3227(96)00069-2.

Sarnthein, M. (1978), Sand deserts during glacial maximum and climatic optimum, *Nature*, *272*, 43–46, doi:10.1038/272043a0.

Sarnthein, M., G. Tetzlaff, B. Koopmann, K. Wolter, and U. Pflaumann (1981), Glacial and interglacial wind regimes over the eastern subtropical Atlantic and North-West Africa, *Nature*, *293*, 193–196, doi:10.1038/293193a0.

Sarnthein, M., K. Winn, S. J. A. Jung, J.-C. Duplessy, L. Labeyrie, H. Erlenkeuser, and G. Ganssen (1994), Changes in East Atlantic Deepwater circulation over the last 30,000 years: Eight time slice reconstructions, *Paleoceanography*, *9*, 209–267, doi:10.1029/93PA03301.

Sarnthein, M. et al. (2001), Fundamental modes and abrupt changes in North Atlantic circulation and climate over the last 60 ky - Concepts, reconstruction, and numerical modelling, in *The Northern North Atlantic: A Changing Environment*, edited by P. Schäfer et al., pp. 365–410, Springer, Berlin, doi:10.1007/978-3-642-56876-3_21.

Schäfer-Neth, C., and A. Paul (2004), The Atlantic Ocean at the Last Glacial Maximum: 2. Reconstructing the current systems with a global ocean model, in *The South Atlantic in the Late Quaternary - Reconstruction of Material Budget and Current Systems*, edited by G. Wefer, S. Mulitza, and V. Ratmeyer, pp. 549–583, Springer, Berlin.

Schefuß, E., S. Schouten, and R. R. Schneider (2005), Climatic controls on central African hydrology during the past 20,000 years, *Nature*, *437*, 1003–1006, doi:10.1038/nature03945.

Schneider, R. R., B. Price, P. J. Müller, D. Kroon, and I. Alexander (1997), Monsoon related variations in Zaire (Congo) sediment load and influence of fluvial silicate supply on marine productivity in the East Equatorial Atlantic during the last 200,000 years, *Paleoceanography*, *12*, 463–481, doi:10.1029/96PA03640.

Shackleton, N. J., M. A. Hall, and E. Vincent (2000), Phase relationships between millennial-scale events 64,000–24,000 years ago, *Paleoceanography*, *15*, 565–569, doi:10.1029/2000PA000513.

Stuut, J.-B., M. Zabel, V. Ratmeyer, P. Helmke, E. Schefuß, G. Lavik, and R. Schneider (2005), Provenance of present-day eolian dust collected off NW Africa, *J. Geophys. Res.*, *110*, D04202, doi:10.1029/2004JD005161.

Tomczak, M. (2003), *Regional Oceanography: An Introduction*, Daya Publ. House, Delhi.

Van Meerbeeck, C. J., H. Renssen, and D. M. Roche (2008), How did Marine Isotope Stage 3 and Last Glacial Maximum climates differ? Perspectives from equilibrium simulations, *Clim. Past Discuss.*, *4*, 1115–1158, doi:10.5194/cpd-4-1115-2008.

Waelbroeck, C., L. Labeyrie, E. Michel, J. C. Duplessy, J. F. McManus, K. Lambeck, E. Balbon, and M. Labracherie (2002), Sea-level and deep water temperature changes derived from benthic foraminifera isotopic records, *Quat. Sci. Rev.*, *21*, 295–305, doi:10.1016/S0277-3791(01)00101-9.

Weltje, G. (1997), End-member modeling of compositional data: Numerical-statistical algorithms for solving the explicit mixing problem, *Math. Geol.*, *29*, 503–549, doi:10.1007/BF02775085.

Weltje, G. J., and M. A. Prins (2007), Genetically meaningful decomposition of grain-size distributions, *Sediment. Geol.*, *202*, 409–424, doi:10.1016/j.sedgeo.2007.03.007.

White, F. (1983), *Vegetation of Africa: A Descriptive Memoir to Accompany the UNESCO/AETFAT/UNSO Vegetation Map of Africa*, *Nat. Resour. Res.*, *20*, 356 pp.

Wien, K., D. Wissmann, M. Kölling, and H. D. Schulz (2005), Fast application of X-ray fluorescence spectrometry aboard ship: How good is the new portable Spectro Xepos analyser?, *Geo Mar. Lett.*, *25*, 248–264, doi:10.1007/s00367-004-0206-x.

Zabel, M., T. Bickert, L. Dittert, and R. R. Haese (1999), Significance of the sedimentary Al/Ti ratio as an indicator for variations in the circulation patterns of the equatorial North Atlantic, *Paleoceanography*, *14*, 789–799, doi:10.1029/1999PA900027.

Zabel, M., R. R. Schneider, T. Wagner, A. T. Adegbie, U. de Vries, and S. Kolonic (2001), Late Quaternary climate changes in Central Africa as inferred from terrigenous input to the Niger Fan, *Quat. Res.*, *56*, 207–217, doi:10.1006/qres.2001.2261.